ORIGINAL RESEARCH ARTICLE

Effect of Laser Energy Density and Scanning Strategy on Residual Stress in Laser Melting Deposited FGH4096 Superalloy

Shuai Liu , Changsheng Liu, and Chao Yuan

Due to the high manufacturing cost, the failure or wear of FGH4096 superalloy parts can be quickly repaired through laser melting deposition (LMD). However, the repeated local rapid heating and cooling processes can increase residual stresses (RS), which reduce the service life of remanufactured parts and even cause cracking. This study analyzed the microstructure and formability of FGH4096 under different laser energy densities and scanning strategies and investigated the RS along the height direction through x-ray diffraction. The results showed that the process parameters had no effect on the phases in the deposited layer, and relatively higher energy density was conducive to obtaining denser samples, while the scanning strategies had little effect on the relative density of the samples. The RS at the top of the cladding layer exhibited tensile stress, while it exhibited compressive stress at the bottom or heat-affected zone. The maximum stress values were related to the process parameters, and lower energy density and an inclined scanning strategy were conducive to reducing the maximum RS and increasing the thickness of the low-stress layer. The research can help design or optimize LMD process parameters for FGH4096 to maximize the relative density of cladding layers while minimizing RS.

1. Introduction

Compared to superalloys produced by traditional ingot metallurgy, powder metallurgy (P/M) superalloys are also based on nickel, supplemented with various alloy elements such as Co, Cr, W, Mo, Al, Ti, Nb, and Ta. However, the distinct difference is that elemental segregation in P/M superalloys can be confined within powder particles, resulting in uniform microstructures and fine grains. Therefore, P/M superalloys exhibit excellent high-temperature strength, fatigue resistance, and resistance to hot corrosion. FGH4096, a second-generation damage-tolerant P/M superalloy, is the preferred material for

Shuai Liu and **Chao Yuan**, Shenyang National Laboratory for Materials Science, Institute of Metal Research, Chinese Academy of Sciences, Shenyang 110016, China; and **Changsheng Liu**, School of Materials Science and Engineering, Key Laboratory for Anisotropy and Texture of Materials Ministry of Education, Northeastern University, Shenyang 110819, China. Contact e-mail: 15040369625@163.com.

the turbine disks of aircraft engines and is also widely used in other rotating components of high-performance engines (Ref 1-3). The composition of FGH4096 is similar to that of René88DT. Compared with the first-generation P/M superalloys (such as René95 and IN100), it reduces the γ' phase content (about 35% by volume), adjusts the grain size, moderately decreases the strength level, and enhances the crack propagation resistance. Furthermore, it raises the maximum service temperature from 650 to 750 °C, endowing the alloy with exceptional comprehensive mechanical properties, along with excellent resistance to corrosion and high-temperature oxidation (Ref 4-6).

However, the superior performance of FGH4096 comes at the cost of elevated manufacturing expenses, which makes repair an appealing alternative for addressing faults or wear in FGH4096 parts. The challenge lies in achieving efficient repairs while ensuring the repaired components meet the required performance and reliability standards. Laser melting deposition (LMD) is an additive manufacturing (AM) technology that utilizes a laser beam to melt metal powder and deposit it layer by layer on the surface of a workpiece, enabling the construction of complex metal components. In comparison with other AM techniques, LMD exhibits numerous unique advantages in applications requiring near-net-shaped components (Ref 7, 8). For instance, LMD technology can be employed to process large parts that cannot be volumetrically built using selective laser melting (SLM). Additionally, LMD is highly effective in repairing damaged or worn parts (Ref 9, 10). This manufacturing process also offers higher deposition rates and a wider processing window, facilitating the optimization of finished components.

In the field of metal AM, attaining optimal formability ranks as the foremost objective for researchers, aiming to produce

crack-free and fully dense deposition layers with a relative density exceeding 99% (Ref 11). The influence of materials, equipment, and processes on the formability of deposition layers is significant. The line energy density (Pt/v, where P is laser power, t is time, and v is scanning speed) is considered a key factor affecting the relative density of deposition layers (Ref 12). In comparison, SLM technology, known for its high precision, typically enables the production of samples with high relative density (even exceeding 99.5%) (Ref 13). However, LMD technology, which offers higher deposition efficiency, faces challenges in achieving higher density.

Furthermore, nickel-based superalloys, especially when aluminum and titanium content exceed 6%, are considered difficult-to-weld alloys and prone to thermal cracking during the AM process (Ref 14, 15). Additionally, a common issue in AM technology is the repetitive cycle of rapid heating and cooling, resulting in unique and complex thermal histories and generating significant residual stresses (RS) (Ref 16). RS are known to limit the wider industrial applications of AM, necessitating effective strategies to mitigate RS in manufacturing and repairing components.

Extensive research has been conducted on RS in the AM process. Various methods are employed to mitigate these RS, including reducing energy input, optimizing scanning strategies, preheating, and post-processing. In a study by Alam et al. (Ref 17), the RS in laser-cladded AISI 420 martensitic stainless steel were analyzed. The researchers reported that higher levels of laser power and speed resulted in increased RS. Another study by Cheng et al. (Ref 18) investigated the effects of different scanning strategies on temperature, RS, and deformation in a three-layer SLM model. They found that the 45°-line scanning strategy exhibited the lowest deformation. However, most studies have primarily focused on the RS at the top surface, providing limited guidance for practical production processes (Ref 19, 20). It is crucial to characterize the RS along the depth in AM processes because the process characteristics determine their distribution, which may differ from the surface. Additionally, there is uncertainty regarding the stress nature (tensile or compressive), which also impacts the mechanical properties of the components.

In this study, we aimed to deposit FH4096 alloy powder utilizing LMD technology. Initially, we optimized the LMD process for FGH4096 alloy, focusing on relative density as a key indicator, and then characterized the microstructure of the deposited FGH4096 alloy. Furthermore, we investigated the effects of varying energy densities and scanning strategies on the RS along the depth of the deposited layers. The results of this research offer theoretical support for the remanufacturing of crucial components made of FGH4096 alloy.

2. Materials and Methods

2.1 Materials and LMD Process

For this experiment, a P/M FGH4096 alloy thick plate was chosen as the substrate. Prior to the experiment, the surface was meticulously cleaned and polished using a grinding machine to eliminate any dirt, revealing a pristine substrate. Afterward, the substrate was thoroughly degreased using alcohol and acetone, followed by a drying process. The received FGH4096 alloy powder had a well-defined composition, as presented in Table 1,

Table 1 Chemical compositions of the received FGH4096 alloy powder (wt.%)

Ni	Cr	Co	Mo	W	Al	Ti
Bal	16.0	12.9	4.0	3.9	2.3	3.7
	Nb	Fe	Zr	C	B	…
	0.8	0.1	0.05	0.04	0.01	…

and its morphology is depicted in Fig. 1. The powder exhibited a relatively uniform particle size distribution with minimal agglomeration, and the majority of particles displayed a near-perfect spherical shape, ensuring compatibility with the LMD process.

To reduce thermal stress, the substrate was preheated to around 400 °C before performing LMD, which is crucial for processing γ' precipitation nickel-based superalloys (Ref 21), including FGH4096. LMD experiments were conducted on a three-axis CNC machine, as shown in Fig. 2. The LMD system consisted of a YAG-1000 W fiber laser provided by IPG in Germany, a coaxial powder feeding device, and a circulating water cooling system. The experiments were conducted under high-purity argon gas protection (99.99%). During the LMD process, a positive defocusing mode with a defocusing distance of 4 mm was used. The corresponding laser spot diameter was 1.8 mm, and the initial laser scanning strategy employed was a non-rotating scan at 0° (referred to as S1).

The laser power to be optimized ranged from 1400 to 2000 W, and the scanning speed ranged from 4 to 6 mm/s. To avoid discussing too many parameters in one study, the overlap rate was kept at 40%, and the powder feeding rate was set at 12 kg/h. Since the layer height of the samples was approximately 0.6 mm, the height increment was set to 0.5 mm for the deposition of 30 layers, resulting in samples with a deposited layer height of approximately 15 mm.

2.2 Measurements

After preparing the samples, the deposited layers along with the substrate were cut into appropriately sized blocks using wire cutting. Firstly, the sample surface was smoothed using 100# sandpaper to remove grooves and oxide layers caused by wire cutting. Then, the samples were mechanically polished and polished further. The surface was etched using a corrosion solution with a volume ratio of HNO_3:HCl:H_2O as 1:2:10. The etched samples were rinsed with alcohol and air-dried.

Microstructural observations of the samples were conducted using an Olympus U-SWB130 metallographic microscope, a JSM-7001F field emission scanning electron microscope, and a JEM-2100F transmission electron microscope (TEM). For TEM samples, double-jet processing was performed using a 10% alcoholic solution of high chloric acid at temperatures ranging from -30 to -20 °C and with a voltage of 30 V. The actual density of the samples was measured using Archimedes' method, and the relative density was obtained by dividing the actual density by the density of the received FGH4096 alloy substrate (8.34 g/cm³). X-ray analysis and RS evaluation of the samples were conducted using a Smartlab-9000 x-ray diffractometer (XRD) with a $Cu\_K\alpha$ line ($\lambda = 1.5406$ Å), a tube voltage of 40 kV, and a tube current of 250 mA. Continuous scanning was used for phase analysis with a scanning step of 0.02°, a scanning range of 20°-100°, and a scanning speed of
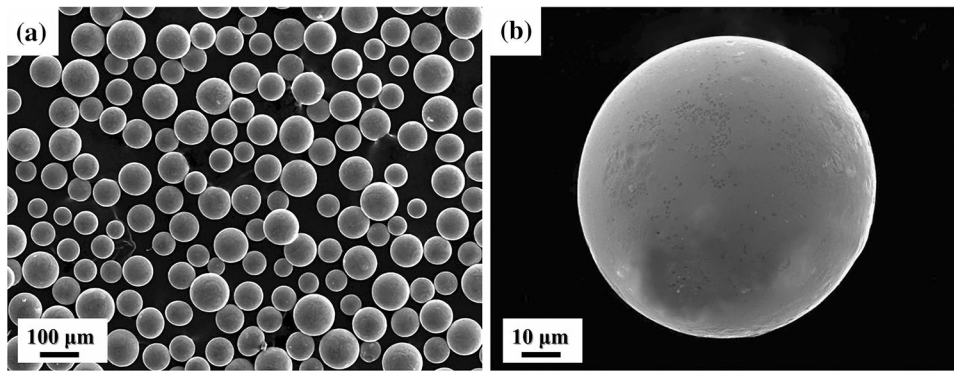
Fig. 1 (a, b) SEM morphology showing the near-perfect spherical FGH4096 alloy particles
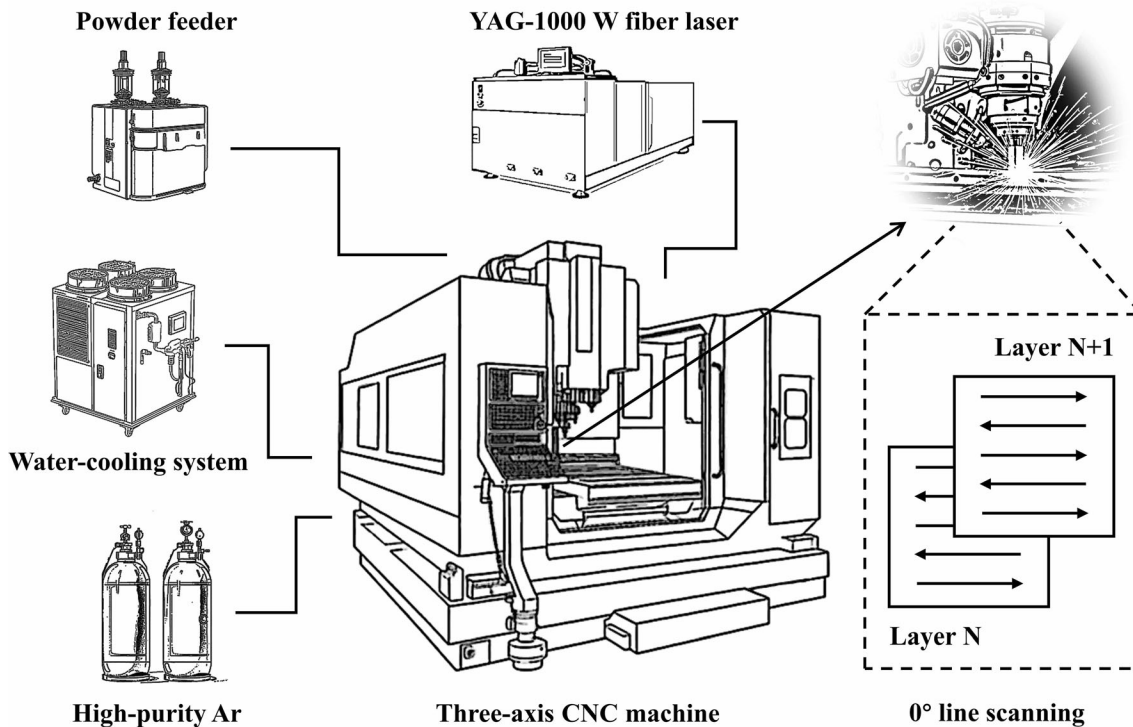
Fig. 2 Schematic diagram of the LMD system and laser scanning strategy

5°/min. Stress evaluation was performed using the $\sin^2 \psi$-method (Ref 22). Stresses (σ_x) and (σ_z) were recorded every 4 mm from top to bottom, including the substrate, to describe the stress distribution. The RS measurements were taken three times, and the average of the three readings was recorded. Before measurement, all samples were immersed in a saturated sodium chloride (NaCl) solution for 1 min to remove any surface oxides.

3. Results and Discussion

The deposition was performed using the 12 process parameters for optimization listed in Table 2, and the relative density is illustrated in Fig. 3. Samples printed with process numbers 1, 4, and 8 exhibited complete densification (relative density > 99%), with corresponding line energy densities

calculated as 350, 360, and 400 J/mm, respectively. This demonstrates the favorable impact of moderately higher line energy density on improving relative density, consistent with the findings reported by Perevoshchikova et al. (Ref 23) The highest relative density (99.42%) was achieved using process number 8. Additionally, it is noteworthy that despite both process numbers 4 and 11 having a line energy density of 400 J/mm, the corresponding samples showed a decrease in relative density with increasing scanning speed, which was also observed in Wang et al.'s study (Ref 13). This phenomenon can be attributed to the promotion of powder splashing with higher scanning speeds (Ref 24). Therefore, it is recommended to select a combination of low power and low scanning speed at the same line energy density.

Figure 4 presents the XRD patterns of samples printed with process numbers 2, 6, 8, and 10, along with the original powder. While the different process parameters do not alter the

Table 2 The detailed process parameters for Fig. 3

Process number	Laser power, W	Scanning speed, mm/s	Linear energy density, J/mm
1	1400	4	350
2	1400	5	280
3	1400	6	233
4	1600	4	400
5	1600	5	320
6	1600	6	267
7	1800	4	450
8	1800	5	360
9	1800	6	300
10	2000	4	500
11	2000	5	400
12	2000	6	333
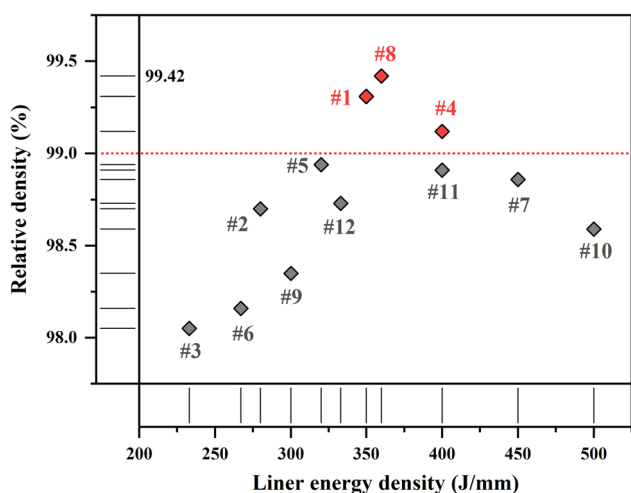
Fig. 3 Relative density of FGH4096 alloy samples deposited with different process parameters
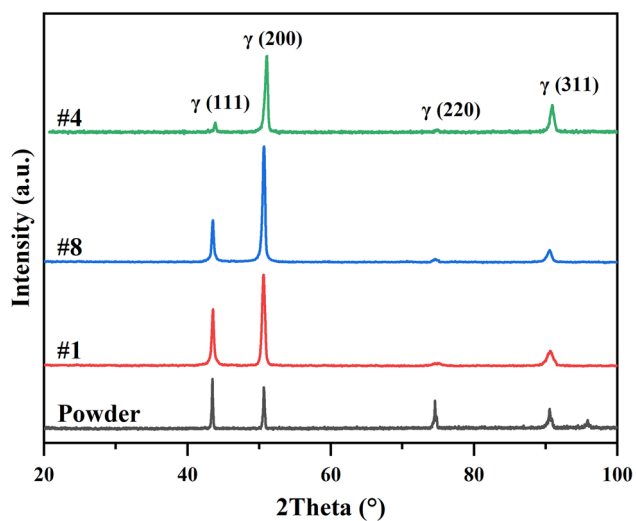
Fig. 4 XRD scans of FGH4096 powder and deposited samples with different process parameters

phase composition, they do affect the intensity of the diffraction peaks corresponding to these phases. The variations in peak intensity for different crystal planes were calculated using the

Table 3 XRD examination of samples revealing its peak characteristics

	Peak intensity ratio, % $[(I/I_{max})^{(hkl)}]$			
Sample type	(111)	(200)	(220)	(311)
Powder	100	86.3	55.8	38.9
#1	62	100	3.1	16.3
#8	36.4	100	2.7	10.6
#4	11.3	100	2.4	34.5

$(I/I$max$)$ (hkl) ratio (Ref 25), as summarized in Table 3. The observed diffraction peaks at approximately 2θ 43.6°, 50.7°, 74.6°, and 90.6° correspond to the (111), (200), (220), and (311) planes of the γ matrix, respectively. Differentiating the γ′ phase from the γ matrix in nickel-based superalloys proves challenging via XRD due to their coherent precipitation and small lattice parameter difference (Ref 26). In comparison with the powder, the deposited samples exhibit a strong texture with a prominent (200) peak, indicating preferential growth during deposition. Moreover, as the energy density increases, this preferential growth becomes more pronounced. Additionally, based on the previous observations, during the solidification process, the γ phase precipitates first in the liquid phase, followed by the enrichment of elements such as C and Ti in the remaining liquid phase. When the segregation of these elements surpasses their solubility limit in the liquid phase, MC-type carbides form in the interdendritic regions (Ref 27). However, no distinct carbide diffraction peaks were detected in the deposited layer, suggesting that rapid cooling hindered carbide formation, resulting in carbide content too low to be detected by x-ray diffraction. Therefore, further characterization and analysis are necessary to investigate the γ′ and carbides in the deposited FGH4096.

Figure 5 shows the microstructure of the FGH4096 sample deposited with process number 8. In Fig. 5(a), the dendrites, represented by dark regions, are the matrix, while the interdendritic regions are the precipitates, accompanied by sporadic white spots. The deposited sample exhibits a fine microstructure, making it difficult to distinguish the precipitates at low magnification. By examining the microstructure between dendrites (Fig. 5b) and within dendrites (Fig. 5c) using TEM, it can be observed that the white spots in Fig. 5(a) are MC

carbides. The interdendritic regions are rich in γ' precipitates, while the γ' within the dendrites is sparser and exhibits a circular contour. Due to rapid cooling, the growth of precipitates in nickel-based superalloys produced through additive manufacturing (AM) is suppressed compared to other processes such as casting and forging. As a result, the γ' size and content are lower and often exhibit a unique circular shape (Ref 28). It is worth noting that no γ/γ' eutectic was found in the deposited FGH4096 sample, which distinguishes it from many high (Al + Ti) nickel-based superalloys, such as IN738.

Furthermore, in Fig. 5(a), three regions can be distinguished from left to right: A, B, and C, corresponding to columnar dendrites, equiaxed dendrites, and irregular dendrites, respectively. In fact, they are all columnar dendrites, but with different growth angles. The middle "equiaxed" dendrites represent a cross-section of the columnar dendrites, with an angle close to 90° relative to the columnar dendrites on the left side. This microstructural pattern is commonly observed in samples scanned without rotation at 0°. This is because the cooling rate decreases as the melt solidifies, resulting in directional solidification (Ref 29). Due to the preferential distribution of undercooling, the nucleation rate is significantly affected, and dendrites grow approximately along the height direction, forming columnar crystals. However, dendrites located at the overlap of layers and tracks experience some deviation in their growth direction, known as oriented dendrites (Ref 30). Since the growth direction of grains is perpendicular to the interface, and the next layer's melt pool interface in the sample with 0° non-rotational scanning is approximately parallel to the previous melt pool interface in space, most of the oriented dendrites with angles close to 90° are formed. This is more visually depicted in Fig. 6(a). Additionally, cracking occurred in the sample, as shown in Fig. 6(b).

Nickel-based superalloys are extensively studied for their cracking mechanisms during the additive manufacturing (AM) process. The commonly recognized cracking mechanisms include solidification cracking (SC), liquation cracking (LC), ductility-dip cracking (DDC), and oxide-induced cracking (Ref 16). However, in our observations of the deposited FGH4096 alloy, γ/γ' eutectics were not present, which eliminates the possibilities of SC and LC since they are closely associated with low-melting constituents such as γ/γ' eutectics and Laves phases. Furthermore, the cracks did not exhibit the distinct characteristics of DDC, which occur at the three-grain boundary intersection with prolonged exposure to the alloy's plasticity reducing temperature (0.5-0.7 $T_{Liquidus}$). Moreover, since the deposition process was carried out in a protective atmosphere and the FGH4096 alloy demonstrated excellent oxidation resistance, oxide-induced cracking can also be ruled out. In our study, cracking was an incidental phenomenon occurring in a small number of samples, primarily in the upper-middle region and only in samples with higher energy densities. Therefore, the only remaining possibility is thermal stress induced during the deposition process. This stress can be attributed to excessive energy input and significant differences in dendrite growth angles caused by the 0° non-rotational scanning strategy. Addressing this issue involves reducing the energy input and modifying the scanning strategy to minimize thermal stress.

Since these incidental cracks occur in the upper-middle region of the deposited layer, we chose to evaluate the RS in the deposition direction. It is worth mentioning that when there are
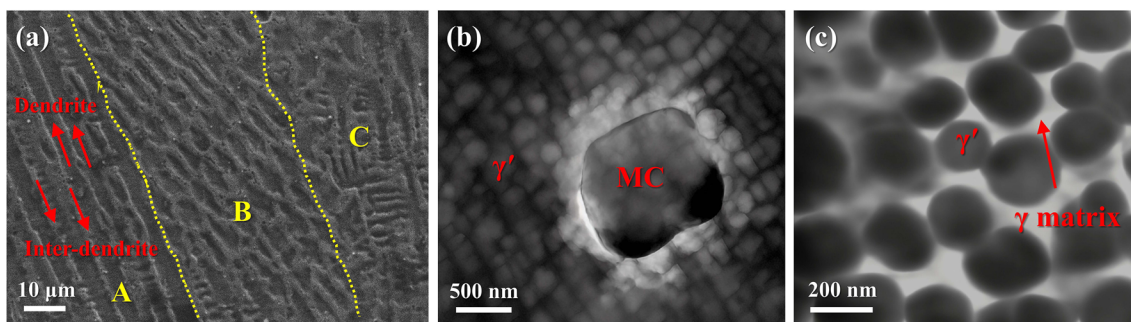
Fig. 5 (a) Low-magnification SEM micrograph of deposited FGH4096 alloy, with high-magnification views of (b) interdendritic region and (c) dendritic precipitates using TEM
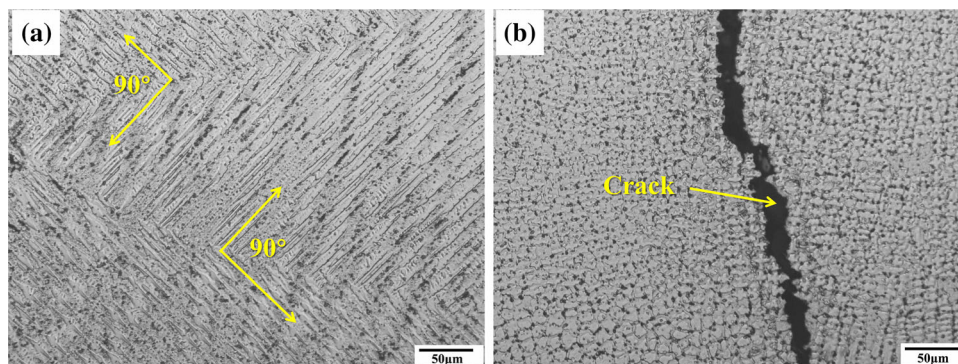
Fig. 6 (a) 90°-oriented dendrites and (b) a crack in the sample
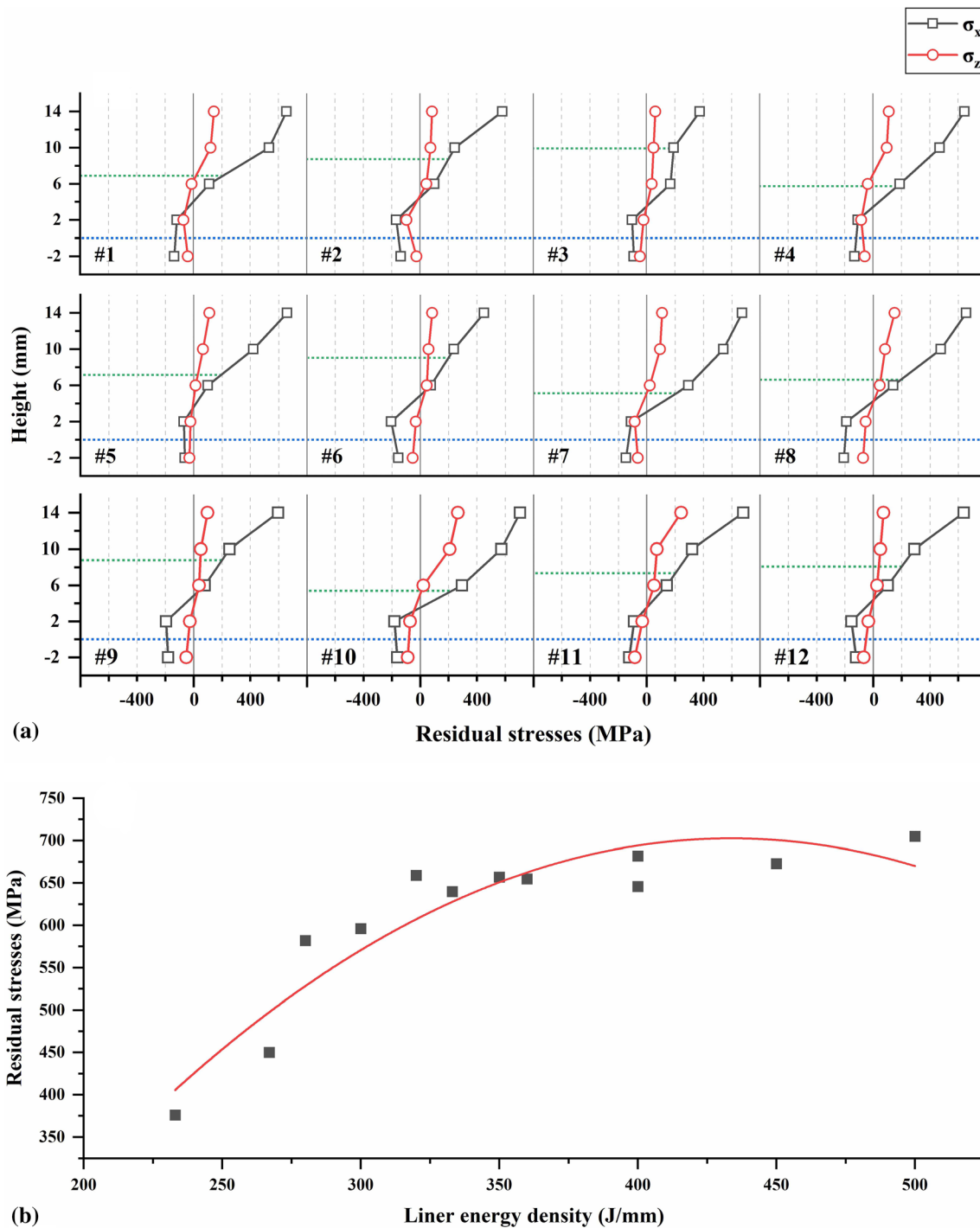
Fig. 7 (a) Longitudinal RS distribution for different process parameters (b) and relationship between maximum tensile stress and energy density

abnormally low-stress values, it indicates the occurrence of cracking, and the stress is released. To avoid affecting the measurement results, we excluded the counts with abnormally low-stress values during the statistics, meaning that the stress distribution of cracked samples was not evaluated. First, we investigated the effect of energy density on the RS, as shown in Fig. 7(a), where the blue dashed line represents the substrate. The RS distribution along the deposition direction in samples printed with different process parameters follows a consistent pattern: compressive stress at the bottom and the heat-affected zone (HAZ), and tensile stress at the top. This is because the lower layers near the substrate initially experience temperature reduction and then shrinkage from the addition of new layers, leading to compression in the lower layers (Ref 31). As the deposition height increases, heat accumulates in the deposition layer, reducing the temperature gradient in the sample. Therefore, compressive stress shows a decreasing trend from the bottom to the top, eventually transitioning into tensile stress at the top layer. Generally, appropriate compressive stress is considered beneficial for the component, while tensile stress is deemed detrimental as it can significantly affect the mechanical properties even if it is not enough to cause cracking (Ref 32).

Additionally, the magnitude of the lateral stress (σ_x) is much larger than that of the axial stress (σ_z), which explains the observation of cracks propagating along the deposition direction. Moreover, if stress below 200 MPa is defined as low stress, the green dashed line in the figure represents the low-stress layer. The energy density can increase the thickness of the low-stress layer. For example, the thickness of the low-stress layer in process number 3 (energy density = 233 J/mm) is close to 10 mm, while in process number 10 (energy density = 500 J/mm), it is less than 6 mm. Figure 7(b) describes the relationship between the maximum tensile stress along the deposition direction and the energy density. Overall, the maximum tensile stress increases with increasing energy density. The minimum value of 376 MPa corresponds to the lowest energy density of 233 J/mm, while the maximum value of 705 MPa corresponds to the highest energy density of 500 J/mm. In fact, their relationship exhibits a quadratic distribution, where the increase in maximum stress (σ_{max}) starts to become gradual when the energy density (E) reaches a certain value. Equation 1 describes the fitted result.

$$\sigma_{max} = -7.38 \times 10^{-3} E^2 + 6.4 E - 685 \qquad \text{(Eq 1)}$$

By calculation, the energy density at the inflection point is determined to be 434 J/mm, which is higher than the energy density of 360 J/mm required to achieve the highest density. To ensure sufficient density of the samples, while keeping the process parameters optimized through energy density unchanged, further reduction of RS is attempted by adjusting the scanning strategy.

Three typical scanning strategies, namely, 90°-line rotation scan (referred to as S2), 45° rotation scan (S3), and 67° rotation scan (S4), were selected from different scanning strategies designed by Cheng et al. (Ref 18), as shown in Fig. 8(a). Before discussing the impact of scanning strategies on RS, it is necessary to ensure that changing the scanning strategy does not decrease the density. Figure 8(b) displays the densities of samples obtained using process numbers 1, 4, and 8 with different scanning strategies, where S1 represents the initial scanning method (0° no rotation). It can be observed that the scanning strategy does not reduce the relative density, and even after changing the strategy, the three process numbers that initially achieved over 99% relative density can still obtain fully dense samples. Although using the S4 scanning strategy can yield higher density samples, the increase is less than 0.1%, indicating that energy density remains the primary factor affecting relative density. Furthermore, the change in scanning strategy does not significantly impact the relationship between energy density and relative density, which generally conforms to the previous pattern, with process number 8 still achieving the highest relative density. Therefore, only process number 8 will be used to analyze the influence of scanning strategies on RS.

Figure 9(a) shows the distribution of RS along the deposition direction for different scanning strategies. Surprisingly, the change in scanning strategy has a much greater impact on RS than the energy density, especially for tilted scanning strategies. Among them, the 67° rotation scan (S4) can significantly reduce RS, particularly σ_x, by halving its value. Additionally, the thickness of the low-stress layer doubles. This result differs slightly from the simulation results of Cheng et al. (Ref 18), who suggested that the 45° rotation scan (S3) is more favorable for obtaining samples with low RS. However, our findings align with the study by Xu et al. (Ref 14), where they also achieved low RS samples by using a 67° rotation scan and successfully suppressed cracking in Inconel 738 alloy during the AM process. The reason is believed to be that the 67° rotation scan is more effective in reducing the aspect ratio of columnar grains and inhibiting the formation of large-angle misoriented dendrites, thereby lowering RS. We also observed similar phenomena in our study, as shown in Fig. 9(b). The 45° rotation scan and 67° rotation scan strategies promote the formation of more small-angle misoriented dendrites due to their specific scanning patterns. When the scanning direction changes at these angles, it introduces more disruptions and interruptions in the growth of columnar grains.
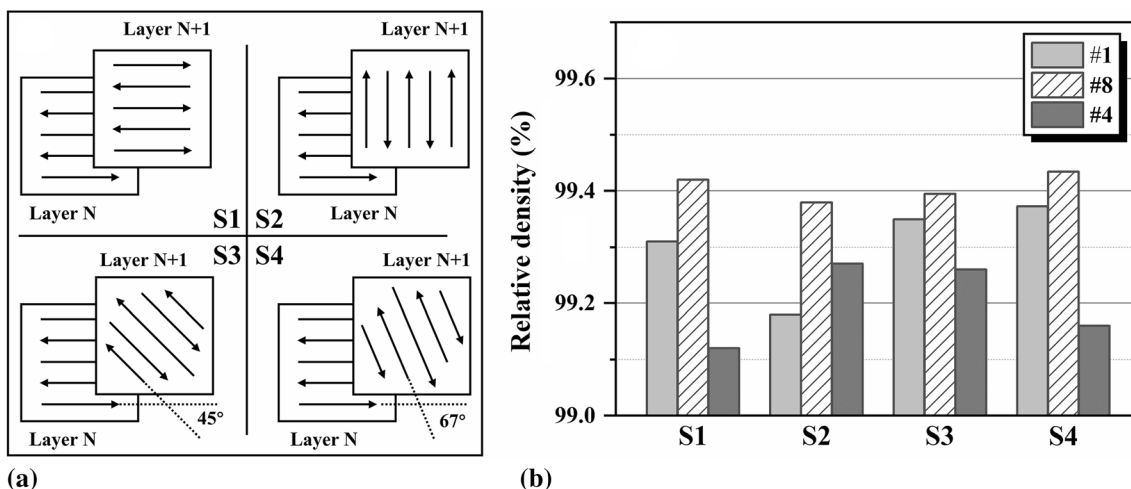
Fig. 8 (a) Scanning strategies of 0°-line rotation scan (S1), 90°-line rotation scan (S2), 45° rotation scan (S3), and 67° rotation scan (S4) and (b) the densities of samples obtained using these scanning strategies
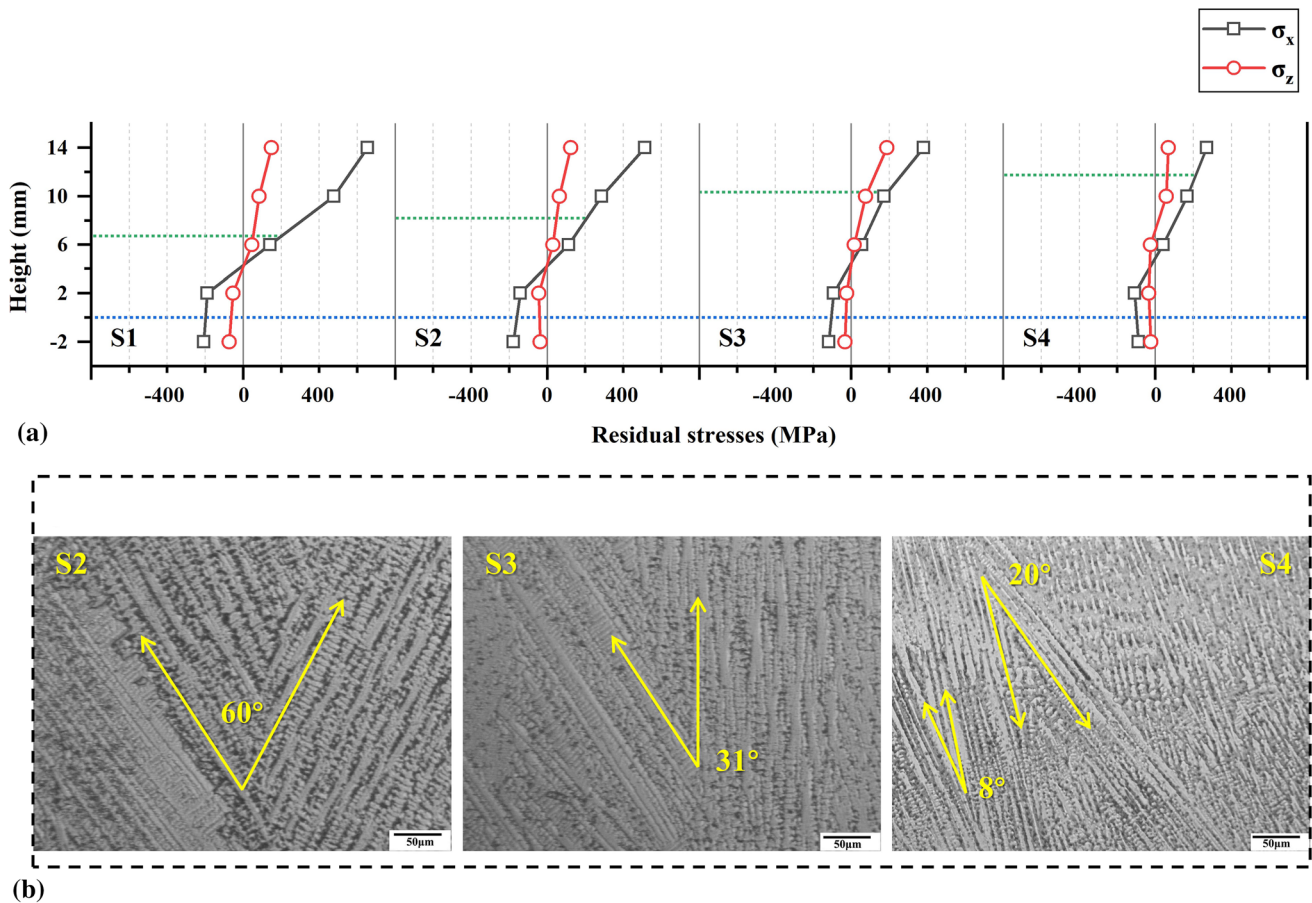
Fig. 9 (a) Longitudinal RS distribution for different scanning strategies and (b) misoriented dendrites with improved scanning strategies

This disrupts the growth front and leads to the formation of smaller and more randomly oriented dendrites. Furthermore, the tilted scanning approach helps redistribute thermal gradients and reduces thermal stress accumulation in specific regions. However, due to the difference in scanning angles, the degree of stress reduction for the 45° rotation scan may be slightly lower compared to the 67° rotation scan. It is worth mentioning that Xu et al. also suggested that the 67° rotation scan strategy promotes dynamic recrystallization, resulting in the formation of local equiaxed grains and causing thermal stress relaxation. However, we did not observe this phenomenon in our study, but even so, its possibility cannot be ruled out and requires further exploration.

Based on the current results, it appears that there is another issue that needs sufficient attention: If the tensile stress at the top increases with height, then in practical repairs, where higher deposition layers are required, this increased tensile stress could potentially severely damage the performance of the repaired part.

To address this, we selected process number 8 and deposited samples with approximately 20 mm (40 layers), 25 mm (50 layers), and 30 mm (60 layers) using a scanning strategy of rotating at 67°. The distribution of RS along the deposition direction for these samples is shown in Fig. 10. It was found that the maximum RS does not increase linearly with the number of deposition layers. The rate of increase becomes smaller, and the maximum RS at the top of the 60-layer sample is only 35 MPa higher than that of the 50-layer sample. This can be understood as the attenuation of the thermal radiation

effect with distance (Ref 31). Therefore, there is no need to excessively focus on the cumulative effect of energy input.

Furthermore, an interesting finding is that the thickness of the low-stress layer increases with the number of deposition layers. In fact, the region with higher stress is limited to the top ten or so layers. Therefore, to obtain a thicker low-stress layer, it is recommended to increase the number of deposition layers.

4. Conclusions

In this study, we employed LMD technology to process FGH4096 alloy powder, optimized laser process parameters, and investigated the microstructure of the deposited FGH4096 alloy as well as the influence of energy density and scanning strategy on RS. The objective was to explore the feasibility of remanufacturing FGH4096 alloy components. The specific conclusions are as follows:

(1) FGH4096 alloy demonstrates good formability during the LMD process, with higher laser energy density leading to denser samples (up to 99.42% density).
(2) Process parameters have less impact on the phases present in the deposited FGH4096 alloy, which primarily consist of γ, γ', and MC carbides.
(3) RS in the deposited layers are tensile at the top and compressive at the bottom.
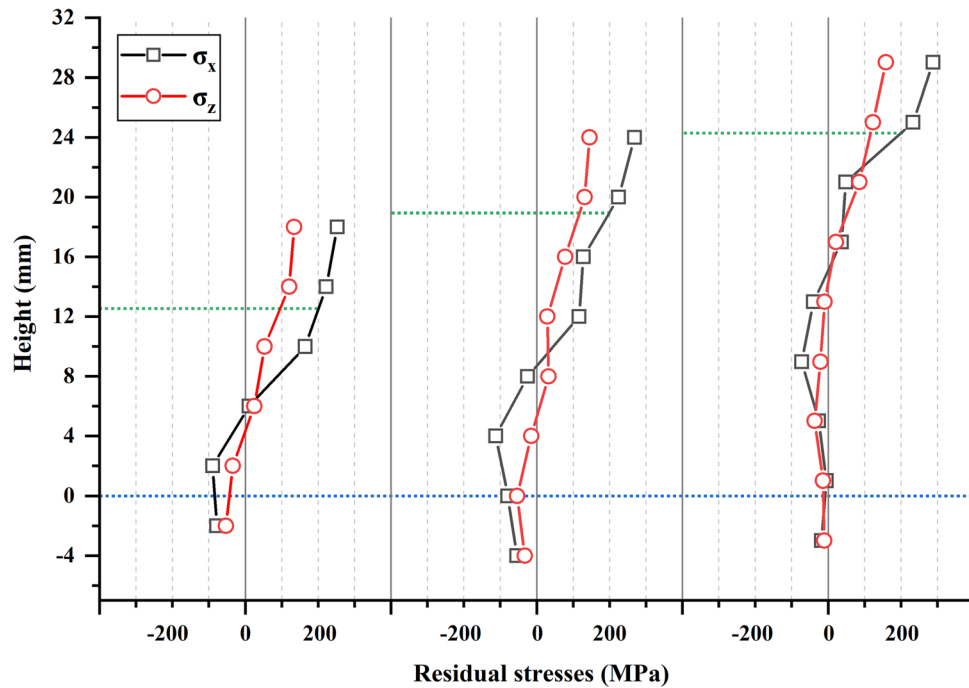
Fig. 10 Longitudinal RS distribution for different deposition heights

(4) The maximum stress in the deposited layers depends on process parameters, with lower energy density and tilted scanning strategies reducing maximum RS and increasing the thickness of the low-stress layer. Changing the scanning strategy, specifically using a rotation angle of 67°, can reduce RS by over 50%.

(5) To achieve thicker low-stress layers in the repaired region, it is recommended to deposit additional layers when reaching the desired repair height.

Acknowledgments

References

1. C. Zhang, W.F. Shen, L.W. Zhang, Y.N. Xia and R.Q. Li, The Microstructure and Gamma Prime Distributions in Inertia Friction Welded Joint of P/M Superalloy FGH96, *J. Mater. Eng. Perform.*, 2017, **26**, p 1581–1588. https://doi.org/10.1007/s11665-017-2601-2

2. A. Liu, Z. Liang, X.S. Wang, W. Xu, Y. Zhang and Y.H. He, Investigation of Fatigue Small Crack Propagation Behavior in Superalloy FGH96 under Different Stress Ratios, *J. Mater. Eng. Perform.*, 2022 https://doi.org/10.1007/s11665-022-07505-w

3. W. Liu, H. Zhang, Z.L. Liu, J.J. Ruan, H.L. Huang, X. Zhou, L.L. Zhu, S.Z. Zhang and L. Jiang, Hot-Working Characteristics and Dynamic Recrystallization Behavior of Hot Isostatically Pressed FGH4096 Superalloy, *Metall. Mater. Trans. A*, 2023, **54**, p 962–982. https://doi.org/10.1007/s11661-022-06951-4

4. Z.B. Hao, T. Tian, X.G. Li, Y.H. Huang, S.Q. Peng, Q. Zhu and C.C. Ge, Effects of Hot Processes on Microstructure Evolution and Tensile Properties of FGH4096 Ni-based Superalloy Processed by Laser Powder Bed Fusion, *Mater. Sci. Eng. A*, 2021, **804**, p140775. https://doi.org/10.1016/j.msea.2021.140775

5. F.L. Li, R. Fu, F.J. Yin, D. Feng, H.Z. Wang, Z.L. Tian, G. Du and Y. Feng, Impact of Solution Heat Treatment on Microstructure and Creep Behavior of a Novel Cast & Wrought FGH4096 Turbine Disk Alloy, *Mater. Sci. Eng. A*, 2017, **696**, p 273–282. https://doi.org/10.1016/j.msea.2017.04.076

6. S.Y. Wang, S. Fang, Z.Z. Shi, J.Y. Jiang, X.M. Zhou and J.G. Lin, Direct Powder Forging of PM Nickel-based Superalloy: Densification and Recrystallisation, *Int. J. Adv. Manuf. Technol.*, 2017, **88**, p 2661–2670. https://doi.org/10.1007/s00170-016-8966-9

7. S.K. Rittinghaus and J. Zielinski, Influence of Process Conditions on the Local Solidification and Microstructure during Laser Metal Deposition of an Intermetallic TiAl Alloy (GE4822), *Metall. Mater. Trans. A*, 2021, **52**, p 1106–1116. https://doi.org/10.1007/s11661-021-06139-2

8. T. DebRoy, H.L. Wei, J.S. Zuback, T. Mukherjee, J.W. Elmer, J.O. Milewski, A.M. Beese, A. Wilson-Heid, A. De and W. Zhang, Additive Manufacturing of Metallic Components—Process, Structure and Properties, *Prog. Mater. Sci.*, 2018, **92**, p 112–224. https://doi.org/10.1016/j.pmatsci.2017.10.001

9. A. Zadpoor, Frontiers of Additively Manufactured Metallic Materials, *Materials*, 2018, **11**(9), p 1566–1576. https://doi.org/10.3390/ma11091566

10. C. Feng, J. Liang, C.Y. Gong, W.Y. Pai and S.F. Liu, Repair Volume Extraction Method for Damaged Parts in Remanufacturing Repair, *Int. J. Adv. Manuf. Technol.*, 2018, **98**, p 1523–1536. https://doi.org/10.1007/s00170-018-2300-7

11. Q. Liu, H.K. Wu, M.J. Paul, P.D. He, Z.X. Peng, B. Gludovatz, J.J. Kruzic, C.H. Wang and X.P. Li, Machine-learning Assisted Laser Powder Bed Fusion Process Optimization for AlSi10Mg: New Microstructure Description Indices and Fracture Mechanisms, *Acta Mater.*, 2020, **201**, p 316–328. https://doi.org/10.1016/j.actamat.2020.10.010

12. A. Foroozmehr, M. Badrossamay, E. Foroozmehr and S. Golabi, Finite Element Simulation of Selective Laser Melting Process considering Optical Penetration Depth of Laser in Powder Bed, *Mater. Des.*, 2016, **89**, p 255–263. https://doi.org/10.1016/j.matdes.2015.10.002

13. H. Wang, X. Zhang, G.B. Wang, J. Shen, G.Q. Zhang, Y.P. Li and M. Yan, Selective Laser Melting of the Hard-to-weld IN738LC Superalloy: Efforts to Mitigate Defects and the Resultant Microstructural and Mechanical Properties, *J. Alloys Compd.*, 2019, **807**, 151662. https://doi.org/10.1016/j.jallcom.2019.151662

14. J. Xu, Y. Ding, Y. Gao, H. Wang, Y. Hu and D. Zhang, Grain Refinement and Crack Inhibition of Hard-to-weld Inconel 738 Alloy by Altering the Scanning Strategy during Selective Laser Melting, *Mater. Des.*, 2021, **209**, 109940. https://doi.org/10.1016/j.matdes.2021.109940

15. X. Zhang, H. Chen, L. Xu, J. Xu, X. Ren and X. Chen, Cracking Mechanism and Susceptibility of Laser Melting Deposited Inconel 738 Superalloy, *Mater. Des.*, 2019, **183**, 108105. https://doi.org/10.1016/j.matdes.2019.108105

16. C. Guo, G. Li, S. Li, X. Hu, H. Lu, X. Li, Z. Xu, Y. Chen, Q. Li, J. Lu and Q. Zhu, Additive Manufacturing of Ni-based Superalloys: Residual Stress, Mechanisms of Crack Formation and Strategies for Crack Inhibition, *Nano Mater. Sci.*, 2022, **5**, p 53–77. https://doi.org/10.1016/j.nanoms.2022.08.001

17. M.K. Alam, A. Edrisy, J. Urbanic and J. Pineault, Microhardness and Stress Analysis of Laser-cladded AISI 420 Martensitic Stainless Steel, *J. Mater. Eng. Perform.*, 2017, **26**(3), p 1–9. https://doi.org/10.1007/s11665-017-2541-x

18. B. Cheng, S. Shrestha and K. Chou, Stress and Deformation Evaluations of Scanning Strategy Effect in Selective Laser Melting, *Addit. Manuf.*, 2016, **12**, p 240–251. https://doi.org/10.1016/j.addma.2016.05.007

19. Y. Huang and X. Zeng, Investigation on Cracking Behavior of Ni-based Coating by Laser-induction Hybrid Cladding, *Appl. Surf. Sci.*, 2010, **256**(20), p 5985–5992. https://doi.org/10.1016/j.apsusc.2010.03.106

20. Y. Xu, L.H. Zhan, L.Z. Xu and M.H. Huang, Experimental Research on Creep Aging Behavior of Al-Cu-Mg Alloy with Tensile and Compressive Stresses, *Mater. Sci. Eng. A*, 2017, **682**, p 54–62. https://doi.org/10.1016/j.msea.2016.11.043

21. J.J. Yan, D.L. Zheng, H.X. Li, X. Jia, J.F. Sun, Y.L. Li, M. Qian and M. Yan, Selective Laser Melting of H13: Microstructure and Residual Stress, *J. Mater. Sci.*, 2017, **52**, p 12476–12485. https://doi.org/10.1007/s10853-017-1380-3

22. N.C. Levkulich, S.L. Semiatin, J.E. Gockel, J.R. Middendorf, A.T. DeWald and N.W. Klingbeil, The Effect of Process Parameters on Residual Stress Evolution and Distortion in the Laser Powder Bed Fusion of Ti-6Al-4V, *Addit. Manuf.*, 2019, **28**, p 475–484.

23. N. Perevoshchikova, J. Rigaud, Jordan, Y. Sha, M. Heilmaier, B. Finnin, E. Labelle and X.H. Wu, Optimisation of Selective Laser Melting Parameters for the Ni-based Superalloy IN-738 LC using Doehlert's Design, *Rapid Prototyp. J.*, 2017, **23**(5), p 881–892. https://doi.org/10.1016/j.addma.2019.05.015

24. H. Zheng, H. Li, L. Lang, S. Gong and Y. Ge, Effects of Scan Speed on Vapor Plume Behavior and Spatter Generation in Laser Powder Bed Fusion Additive Manufacturing, *J. Manuf. Processes.*, 2018, **36**, p 60–67. https://doi.org/10.1016/j.jmapro.2018.09.011

25. H. Pouraliakbar, M.R. Jandaghi and G. Khalaj, Constrained Groove Pressing and Subsequent Snnealing of Al-Mn-Si Alloy: Microstructure Evolutions, Crystallographic Transformations, Mechanical Properties, Electrical Conductivity and Corrosion Resistance, *Mater. Des.*, 2017, **124**, p 34–46. https://doi.org/10.1016/j.matdes.2017.03.053

26. A. Ramakrishnan and G.P. Dinda, Direct Laser Metal Deposition of Inconel 738, *Mater. Sci. Eng. A*, 2019, **740–741**, p 1–13. https://doi.org/10.1016/j.msea.2018.10.020

27. J.J. Xu, X. Lin, P.F. Guo, X.L. Wen, Q.G. Li, H.O. Yang and W.D. Huang, HAZ Liquation Cracking Mechanism of IN-738LC Superalloy Prepared by Laser Solid Forming, *Metall. Mater. Trans. A*, 2018, **49**, p 5118–5136. https://doi.org/10.1007/s11661-018-4826-6

28. R. Sidhu, O. Ojo and M. Chaturvedi, Microstructural Analysis of Laser-Beam-Welded Directionally Solidified INCONEL 738, *Metall. Mater. Trans. A*, 2007, **38**, p 858–870. https://doi.org/10.1007/s11661-006-9063-8

29. L. Ren, Y.H. Cheng, R. Shao, X.L. Meng, J.Y. Yang and Q.Q. Wang, DFT Studies of Adsorption Properties and Bond Strengths of H2S, HCN and NH3 on Fe (1 0 0), *Appl. Surf. Sci.*, 2020, **500**, 144232. https://doi.org/10.1016/j.apsusc.2019.144232

30. A. Hattal, T. Chauveau, M. Djemai, J.J. Fouchet, B. Bacroix and G. Dirras, Effect of Nano-yttria Stabilized Zirconia Addition on the Microstructure and Mechanical Properties of Ti6Al4V Parts Manufactured by Selective Laser Melting, *Mater. Des.*, 2019, **180**, 107909. https://doi.org/10.1016/j.matdes.2019.107909

31. Y. Liu, Y. Yang and D. Wang, A Study on the Residual Stress during Selective Laser Melting (SLM) of Metallic Powder, *Int. J. Adv. Manuf. Technol.*, 2016, **87**, p 647–656. https://doi.org/10.1007/s00170-016-8466-y

32. Y.H. Cheng, C.M. Cao, X.Y. Yang, J.L. Zhou, J.Y. Yang, X.B. Liang and X.S. Li, Effects of Laser Energy Density and Path on Residual Stress of Remanufactured Key Components for Shield Tunneling Machine, *Mater. Chem. Phys.*, 2022, **290**, 126617. https://doi.org/10.1016/j.matchemphys.2022.126617